Materials Science & Engineering A 844 (2022) 143174

Contents lists available at ScienceDirect

Materials Science & Engineering A

journal homepage: www.elsevier.com/locate/msea

Anisotropic behaviours of LPBF Hastelloy X under slow strain rate tensile testing at elevated temperature

Cheng-Han Yu [a,*], Ru Lin Peng [a], Tung Lik Lee [b], Vladimir Luzin [c,d], Jan-Erik Lundgren [e], Johan Moverare [a]

[a] Department of Management and Engineering, Division of Engineering Materials, Linköping University, Linköping, SE, 58183, Sweden
[b] ISIS Neutron Facility, STFC Rutherford Appleton Laboratory, Harwell Campus, Didcot, OX11 0QX, Oxfordshire, United Kingdom
[c] Australian Nuclear Science and Technology Organization (ANSTO), Lucas Heights, NSW, 2234, Australia
[d] School of Engineering, The University of Newcastle, Callaghan, NSW, 2308, Australia
[e] Siemens Energy AB, Finspång, SE, 61231, Sweden

ARTICLE INFO

Keywords:
Creep
Slow strain rate tensile testing (SSRT)
Time-of-flight neutron diffraction
Texture
Ductility
Elastic constants

ABSTRACT

To improve the understanding of high temperature mechanical behaviours of LPBF Ni-based superalloys, this work investigates the influence of an elongated grain structure and characteristic crystallographic texture on the anisotropic tensile behaviours in LPBF Hastelloy X (HX) at 700 °C. Two types of loading conditions have been examined to analyse the anisotropy related to the building direction (BD), including the vertical loading (loading direction//BD) and the horizontal loading (loading direction ⊥ BD). To probe the short-term creep behaviours, slow strain rate tensile testing (SSRT) has been applied to address the strain rate dependent inelastic strain accumulation. In-situ time-of-flight neutron diffraction upon loading was performed to track the anisotropic lattice strain evolution in the elastic region and the texture evolution in the plastic region. Combined with the post microstructure and fracture analysis, the anisotropic mechanical behaviours are well correlated with the different microstructural responses between vertical and horizontal loading and the different strain rates. A better creep performance is expected in the vertical direction with the consideration of the better ductility and the higher level of texture evolution.

1. Introduction

Ni-based superalloys are an important group of materials for load bearing applications at extreme conditions, including high temperature and severe corrosion. The excellent mechanical performance makes these materials widely used for the gas turbine applications in aerospace and energy industries [1]. In the recent years, the potential of additive manufacturing (AM) of Ni-based superalloys has increased with the gradually maturing of the AM techniques, and various extended applications have been developed due to the design freedom benefited from AM [2–5]. To ensure robust high temperature applications of AM, this work conducts a fundamental study on the anisotropic tensile behaviours and short-term creep resistance of Hastelloy X (HX) manufactured by laser powder bed fusion (LPBF).

HX is a Ni-based superalloy that is strengthened by carbide precipitation and solid-solution strengthening, and the face-centred cubic (FCC) phase remains stable at elevated temperatures [6]. The combination of excellent corrosion resistance and strength makes HX a good material candidate for components in the hot sections of gas turbines [7]. For powder bed fusion (PBF), it is common to find elongated grain structures and a characteristic texture caused by directional energy input. The texture of PBF FCC materials varies with the different process parameters, such as the different input energy source between laser and electron beam [8], the variation of laser power and laser scan speed [9,10], and the different deposition strategies [11,12]. Although diverse texture and grain structure are revealed under different process parameters, a roughly elongated grain structure can still be found in most LPBF FCC materials, and it is assumed to be responsible for the anisotropic mechanical behaviours. To a general study on the effect of elongated grain structure and texture, the specimens in this work were fabricated by using the standard process in a common LPBF equipment, EOS M290.

Creep performance is one of the important properties for high temperature applications. However, most of the database for the creep

* Corresponding author.
E-mail addresses: cheng-han.yu@liu.se, chenghan.hank.yu@gmail.com (C.-H. Yu).

https://doi.org/10.1016/j.msea.2022.143174
Received 19 January 2022; Received in revised form 15 April 2022; Accepted 18 April 2022
Available online 22 April 2022

properties of HX is from the conventionally manufactured specimens [13–16], and the literature on the creep performance of LPBF HX is scarce [17]. Tensile tests at elevated temperatures can be indirect evidences for the estimation of creep performance, yet, still only limited work on LPBF HX can be found [18–23]. To probe the short-term creep resistance, slow strain rate tensile testing (SSRT) is a useful method [24–26]. With the slow strain rate at the reasonable temperature for the thermally activated process, creep damage will be continuously accumulated after reaching the creep stress. Hence, the strain rate dependent inelastic strain accumulation can be addressed. In our previous study on high temperature tensile behaviours of LPBF HX [23,27], we observe that the grain boundaries become weaker at elevated temperature and a significant ductility loss takes place at 700 °C under a strain rate of 10^{-3}/s. In the continuous work, the significant creep damage associated with the applied slow strain rate of 10^{-5}/s and 10^{-6}/s was investigated [28]. For the slow strain rate of 10^{-5}/s and 10^{-6}/s, continuous softening right after yielding caused by creep damage was observed, which is a significant difference to the strain rate of 10^{-3}/s. The elongated grain structure and the anisotropic texture directly lead to anisotropic tensile behaviours, especially the ductility difference related to the building direction (BD). In addition, deformation twinning has been reported as a mechanism influencing the tensile behaviour of LPBF HX at both room temperature [29,30] and elevated temperature [28], hence, the strain-rate dependence will be investigated in this study.

For creep loading, the heterogeneity of strain distribution is highly related to the localized strain accumulation and slip transmission at grain boundaries [16]. A higher level of heterogeneous strain distribution is expected in LPBF HX due to the characteristic microstructure, and the effect on the mechanical behaviours can be revealed by the lattice strain evolution upon loading. In-situ time-of-flight (TOF) neutron diffraction is a powerful tool to trace multiple lattice plans simultaneously, which is beneficial for deformation mechanism investigation, such as stress partitioning behaviours [31–35] texture evolution [36], and deformation twinning [37,38]. As neutrons can penetrate a large thickness of Ni-based superalloys, the measured full neutron diffraction pattern is beneficial to determine material properties at lattice scale but also generates a good statistical characterization of the bulk material. A higher level of heterogeneous strain distribution is expected in LPBF HX due to the characteristic microstructure, and the effect on the mechanical behaviours can be revealed by the lattice strain evolution upon loading.

In this work, an in-situ TOF neutron diffraction experiment was performed under mechanical loading to address the anisotropic elastic and plastic responses of LPBF HX at 700 °C with two different applied strain rates (10^{-3}/s and 10^{-5}/s). The strain rate of 10^{-5}/s was chosen due to the similar behaviours to the strain rate of 10^{-6}/s. In addition, less creep damage generated during neutron diffraction measurement can be achieved with the faster strain rate. By using Rietveld method for diffraction peak analysis [39], each individual crystallographic lattice response at different loading stage can be obtained [34,40,41]. Combined with post analysis of microstructure of the deformed specimen, the anisotropic deformation and fracture mechanisms of LPBF HX spanning over a wide range of length scales are investigated. Due to the limited accessibility to neutron experiments and the rare capability of in-situ mechanical loading at elevated temperatures, this study provides a unique perspective on the anisotropic deformation behaviours of LPBF FCC materials.

2. Experiments

2. 1Additive manufacturing

Rod-like samples were manufactured by using the standard process of laser powder bed fusion in an EOS M290 equipment. The schematic illustration of the LPBF process can be found Yu's thesis [42]. The rods were 18 mm in diameter and 120 mm in length. The building layer thickness was 40 μm and a scanning rotation of 67° has been applied. For each layer, the hatching was applied first and followed by two lines of contouring with a width of 150 μm.

Two types of rods were built for the purpose of investigating the influence of loading direction (LD). One type was built vertically, with the building direction (BD) parallel to the load direction. Another type was built horizontally, where the loading direction is in the in-plane direction of the powder bed, and the BD is perpendicular to the length of the rod. The powder for the printing was EOS NickelAlloy HX, and the nominal composition can be found in Table 1. The samples for microstructure characterization and mechanical testing are all in the as-built state without any post processing.

2. 2.Mechanical testing

Tensile tests with two different strain rates, 10^{-3}/s and 10^{-5}/s, were performed at 700 °C by using an Instron 5582–100 KN universal testing machine in the lab at Linköping University. The procedure of tensile tests at elevated temperature followed the standard ISO 6892-2. An Instron 7361C extensometer with a gauge length of 12.5 mm was attached at the centre of the tensile specimens. Load cell and extensometer comply with standards ISO 7500-1 (system class 0.5) and ISO9513 (system class 1.0), respectively. Displacement and speed calibrations are performed in accordance with Instron's internal procedure. The applied strain was recorded by the extensometer up to the strain of 0.05 mm/mm, and the rest was calculated from the cross-head displacement. The entire tensile specimen was positioned in a heating chamber with a pre-load of 100 N for the purpose of sample alignment, and a type K thermocouple was attached at the centre of the tensile specimen for the temperature monitoring and control with a maximum variation of ±2 °C during the entire test. The tensile specimen was heated up with a ramp rate of 20 °C/min, and a dwell time of 1 h was applied before the test for the purpose of temperature homogenization.

Cylindrical dog bone tensile specimens were machined from the LPBF rods mentioned in the previous section, and the specimen dimensions are given in Fig. 1. The "vertical loading" (VL) refers to the loading that is applied along the BD, and the "horizontal loading" (HL) refers to the loading that is perpendicular to the BD. In combination with two strain rates, 10^{-3}/s and 10^{-5}/s, there were four loading conditions in total, and the abbreviations of each loading condition are given in Table 2. Due to the limited number of tensile specimens, only one test of each condition was performed. The Young's modulus is determined by applying the linear regression at the elastic regime, and the uncertainty refers to the fitting error.

2. 3TOF in-situ neutron diffraction

In-situ TOF neutron diffraction measurements were performed upon uniaxial tensile loading at 700 °C by using the third-generation ENGIN-X strain diffractometer at the ISIS spallation neutron source, Rutherford Appleton Laboratory, [43]. The experimental data can be found via the ISIS experiment number, RB2010043 [44]. The incident beam is a pulsed neutron beam with an energy range. As the flight path is fixed in the setup of TOF diffraction, the detector records the detected neutrons as a function of time, which can be transferred to wavelength and further to the d-spacing of each {hkl} plane.

The setup for instrument and sample is shown in Fig. 2a. The stress rig was mounted horizontally with the loading axis oriented at 45° to the

Table 1
Nominal composition of the powder EOS NickelAlloy HX, in wt %.

Ni	Cr	Fe	Mo	W	Co	C	Si
Bal.	20.5–23	17–20	8–10	0.2–1	0.5–2.5	≤0.1	≤1
Mn	**S**	**P**	**B**	**Se**	**Cu**	**Al**	**Ti**
≤1	≤0.03	≤0.04	≤0.01	≤0.005	≤0.5	≤0.5	≤0.15

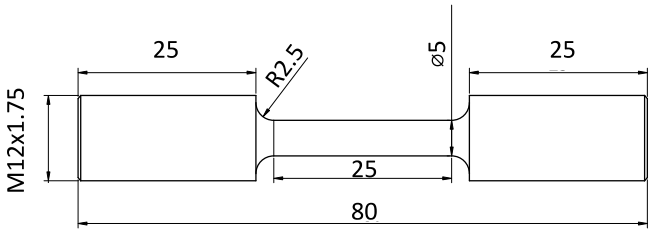

Fig. 1. Geometry of the tensile specimen tested in the lab at Linköping University. Note that the dimensions are in mm.

Table 2
The abbreviations of each loading condition. The variables include the two different loading directions and two different strain rates.

	Vertical loading	Horizontal loading
Strain rate: 10^{-3}/s	V_E-3	H_E-3
Strain rate: 10^{-5}/s	V_E-5	H_E-5

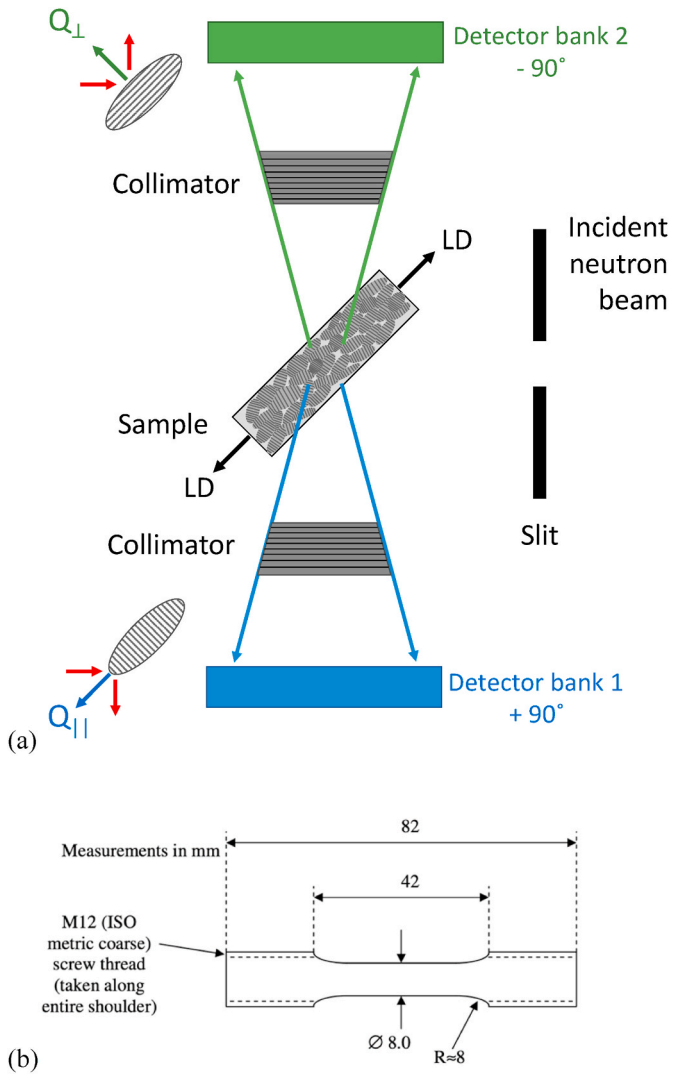

Fig. 2. *(a) The setup of in-situ neutron diffraction measurement upon tensile loading. $Q_{\perp}$ and $Q_{||}$ are the scattering vectors in the LD and RD, respectively. (b) Geometry of the tensile specimen for the stress rig in ENGIN-X* [46].

incident beam. The two detector banks at $2\theta = \pm 90^{\circ}$ enable simultaneous measurement of strains or d-spacing evolution in both the loading direction (LD) and the radial direction (RD). The tensile specimen geometry and dimensions are shown in Fig. 2. To maximize diffracted signal, a large gauge volume defined by the incident beam slit (8 mm in height and 4 mm in width) and the radial collimator (4 mm) was used. The sample was carefully aligned to ensure that the centroid of the gauge volume is positioned at the centre of the specimen gage length. A radiant furnace was mounted on the stress rig to heat the specimen up to 700 °C. The specimen was applied with a small preload of 5 MPa before and during heating. Upon reaching 700 °C, the specimen was held at this temperature for 5 min before diffraction measurements were performed with an acquisition time of about 2 min. This relatively short acquisition time was employed to minimize creep and give a satisfactory diffraction pattern quality. The specimen was then held at the designated applied loads while diffraction measurements were performed. In the initial elastic regime, the tensile loading was stress-controlled. The applied stress rate was determined from the stress-strain curve obtained at the laboratory in Linköping University, as mentioned in the previous section. Each test condition shows a linear response in the elastic regime and hence, the applied stress rate was calculated from the Young's modulus of each stress strain curve respectively. When the loading approached the yielding point, the tensile loading was switched to be strain-controlled in the elasto-plastic regime and plastic regime until failure.

The first measured diffraction pattern is considered as the stress-free state of the specimen, where the stress-free d-spacing, d_0, is taken. The d-spacing of each peak is obtained by peak fitting using Rietveld refinement with the OpenGenie program [45]. The lattice strain is determined by the peak shift of d-spacing,

$$\varepsilon_{hkl} = \frac{d_{hkl} - d^0_{hkl}}{d^0_{hkl}} \quad (1)$$

where ε_{hkl} is the lattice strain of the {hkl} planes and d_{hkl} is the interplanar lattice spacing of the {hkl} plane. The strain measurement uncertainty of ENGIN-X is 50 μ ε (1 μ ε = 10^{-6}) [43].

2. 4Microstructure and texture analysis

The microstructure of the as-built specimen was imaged from the centre of the rod using a Hitachi SU 70 field emission scanning electron microscope (FE-SEM) equipped with an Oxford EBSD (electron back scattered diffraction) detector. The area of interest was polished from 500 Grit down to 4000 Grit, and then fine polishing with diamond suspension was applied from 3 μm down to 0.25 μm. OP-U colloidal silicon suspension was used after the fine polishing followed by the water polishing as the final step. The grain orientation maps were obtained by using EBSD with the applied voltage of 20 kV and the scanning step size of 1 or 0.5 μm depending on the required resolution. The grain size is determined from the high angle grain boundaries (>10°) in the EBSD grain orientation map, which the sectional area of a grain is postulated as a circle and the grain size refers to the equivalent diameter.

The bulk texture of the as-built rod was analysed from the pole figures (PF) measured by using KOWARI, a neutron diffractometer at Australian Nuclear Science and Technology Organization, ANSTO [47]. A monochromatic beam with a wavelength of 1.5 Å was used for the measurement on an approximately 5° × 5° spherical grid, with measurement time of 5 s per angular position. For the neutron texture experiment, coupon cylinders of 10 mm height and 10 mm in diameter (cut from the longer cylinders of 18 mm in diameter) was measured and being fully submerged in the neutron beam. Five PFs were obtained for the sample, including (111), (200), (220), (311) and (222). An open source MATLAB toolbox MTEX was used for the pole figure analysis, texture (orientation distribution function) reconstruction and Young's modulus tensor calculation [48].

For the deformation and fracture mechanism investigation, the

deformed microstructure and fracture surfaces were analysed for the deformed specimens from the tensile tests performed in the lab at Linköping University. The deformed microstructure from the in-situ neutron diffraction experiment at ENGIN-X were not studied in this work due to the reason of extra creep damage accumulated during the holding time for the neutron measurement. The fractography was performed with a combination of light optical microscope (LOM) and FE-SEM for a wide range of length scales. The deformed microstructure was analysed from the cross-section close to the fracture surface; the grain orientation map was taken from the area that was about 1 mm below the fracture, and the step size of 0.5 μm was used for increasing the resolution to reveal the narrow deformation twins.

3. Results

3. 1As-built microstructure

The as-built microstructures and texture are shown in Fig. 3. Elongated grain structure along the BD and a clear Goss-type texture of the as-built LPBF HX are found. From the top view cross-section (a), equiaxed grains reveal the in-plane equiaxiality while the elongation and grain size in this direction are clearly visible in the side view (b). The grain size distribution shows large spread, and the grains can be as large as over 100 μm. From Fig. 3a, a clear <011>//BD (appears in green colour) texture component is exhibited. The same result is demonstrated by the texture measured by using neutron diffraction shown in Fig. 3c, which gives a better statistical quality. While in general the texture is characterized by Goss component, {011}<001>, it has also a noticeable orientation spread around BD approximately ±10°. A further clarification of GOSS-type texture in LPBF microstructure can be found in Bahshwan et al. [49]. Since the side view (b) is mapped from the plane of horizontal loading, it is able to indicate the horizontal loading direction in the pole figures in Fig. 3c by comparing the texture components between two measurements.

3. 2Mechanical behaviours

The tensile tests at two different strain rates were performed at 700 °C. The stress-strain curves are shown in Fig. 4 and the mechanical properties are listed in Table 3. For the strain rate of 10^{-3}/s, the horizontal sample shows higher yield stress, ultimate tensile stress (UTS) and work hardening rate, but the ductility is worse than the vertical sample. On the other hand, for the strain rate of 10^{-5}/s, a continuous softening takes place right after the yield point for both loading directions, and a larger degree of softening is found in the vertical loading. At the slow strain rate, the vertical ductility is still better than the horizontal

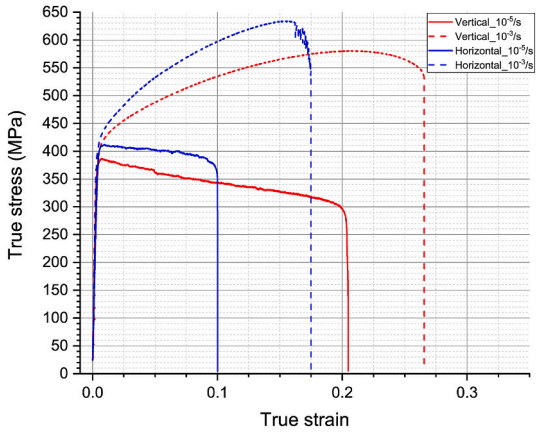

Fig. 4. Four stress - strain curves obtained from the tensile tests at 700 °C performed at the lab in Linköping University. The solid and dotted lines represent the strain rate of 10^{-5}/s and 10^{-3}/s respectively. The red and blue colour refer to the vertically and horizontally built specimens respectively. (For interpretation of the references to colour in this figure legend, the reader is referred to the Web version of this article.)

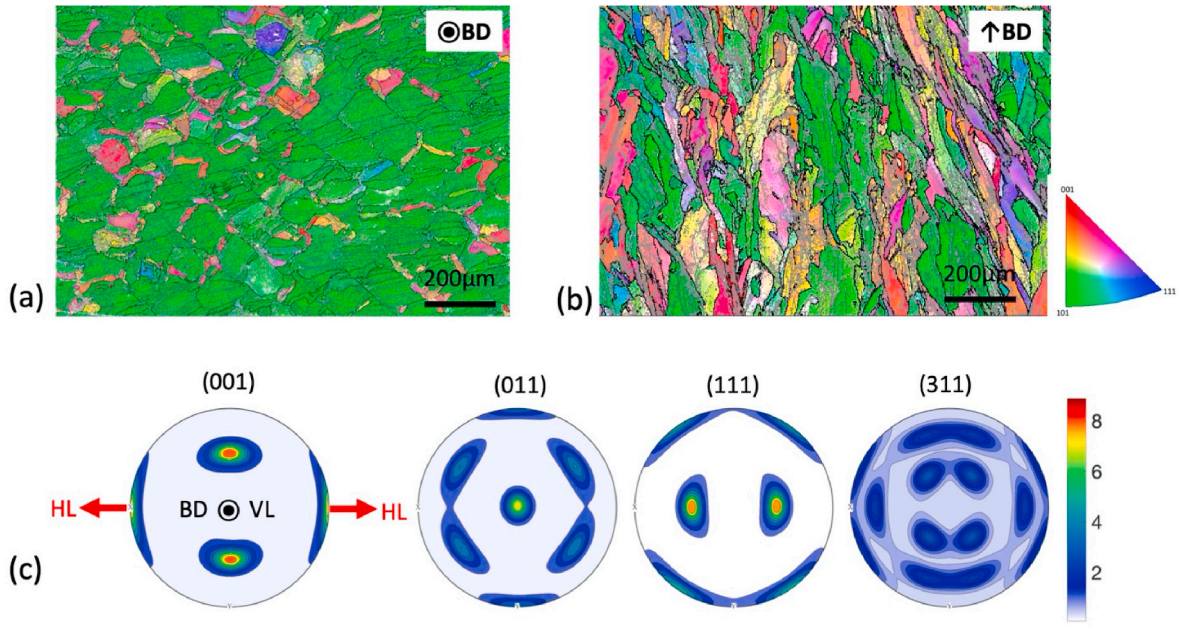

Fig. 3. EBSD grain orientation mapping and texture analysis from neutron diffraction of the as-built LPBF HX. (a) The top view of the microstructure imaged from the vertical loading cross section where the BD is given. (b) The side view of the microstructure imaged from the horizontal loading cross section where the BD is given, and the plane-normal is the horizontal loading direction. Note that the colour legend of both grain orientation maps is according to the BD; the black lines refer to >10° grain boundaries, and the grey lines refer to the >2° grain boundaries. A scanning step size of 1 μm was used for the EBSD setup. (c) The (001), (011), (111) and (311) pole figures of the as-built bulk texture measured by using neutron diffraction at KOWARI. The measured coupon cylinder is from the vertically built rod. The centre of each pole figure refers to the BD. Note that the VL was applied along the BD, which is the centre direction in the pole figures, while the HL was applied along the east-west direction in the pole figures. (For interpretation of the references to colour in this figure legend, the reader is referred to the Web version of this article.)

Table 3
Summary of the mechanical properties at 700 °C for the four different tensile test conditions.

	Yield stress (0.2%), MPa	Young's modulus, GPa	UTS, MPa	Elongation, %	Reduction of area, %
V_E-5	380	113.8 ± 0.15	387	21	45
H_E-5	405	94.3 ± 0.05	412	10	24
V_E-3	395	143.3 ± 0.9	581	27	49
H_E-3	410	138.8 ± 1.14	634	18	26

ductility, and the anisotropy in ductility becomes larger as the ratio of vertical ductility over horizontal ductility increases roughly from 1.5 up to 2. Significant necking is observed in the vertically deformed specimen that leads the higher area reduction, and a slightly higher area reduction is found for the strain rate of 10^{-3}/s.

3. 3In-situ neutron diffraction

The stress-strain curves from the in-situ neutron diffraction measurements are shown in Fig. 5a. The difference in work hardening and softening between the two strain rates is in the same trend as the continuous tensile tests shown in Fig. 4. However, significant stress relaxation occurred during each 2 min neutron measurement period at elevated temperature of 700 °C, especially for the strain rate of 10^{-3}/s. In addition, an inevitable strain accumulation with constant applied stress is evident while the stress-controlled mode is switched to the strain-controlled mode in the elasto-plastic regime.

The lattice strain evolutions in both the LD and the RD at elevated applied stress are plotted in Fig. 5b–e. The lattice elastic constants of different grain families with (hkl) planes oriented in the loading direction can be evaluated from the linear regime of the slope and they are summarized in Table 4. For the lattice strain evolution in the LD, <111> exhibits the highest stiffness while <200> is the softest. In addition, different elastic responses of different (hkl) families at slow strain rate are found. The bulk Young's modulus decreases at the slow strain rate while the elastic constants of <111> and <220> increase significantly in both V_E-5 and H_E-5. For the elastic constant of <200>, only V_E-5 increases at the slow strain rate while H_E-5 remains at the same level.

3. 4Deformed microstructure

The deformed microstructures of V_E-5 and H_E-5 that are close to the fractures are shown in Fig. 6a and b. The higher amount of creep voids in the V_E-5 indicates more creep damage, which agrees with the higher level of softening behaviour shown in Fig. 4. On the contrary, the creep damage in the horizontal loading is considered to concentrate on a major intergranular fracture along the fracture surface, due to less creep voids found in the cross-section and a more continuous intergranular fracture shown in Fig. 7d. On the distribution of the creep voids in V_E-5, a tendency for a "V" shape of creep voids can be found at the top or the bottom of the elongated grains shown in Fig. 6a. A further analysis on the grain orientation map is shown in Fig. 6c and d, the creep voids

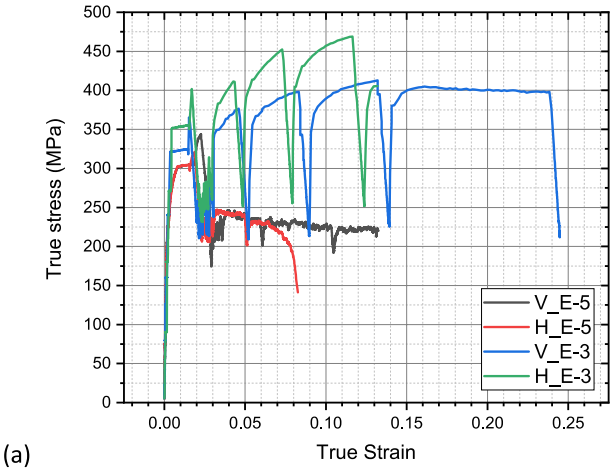

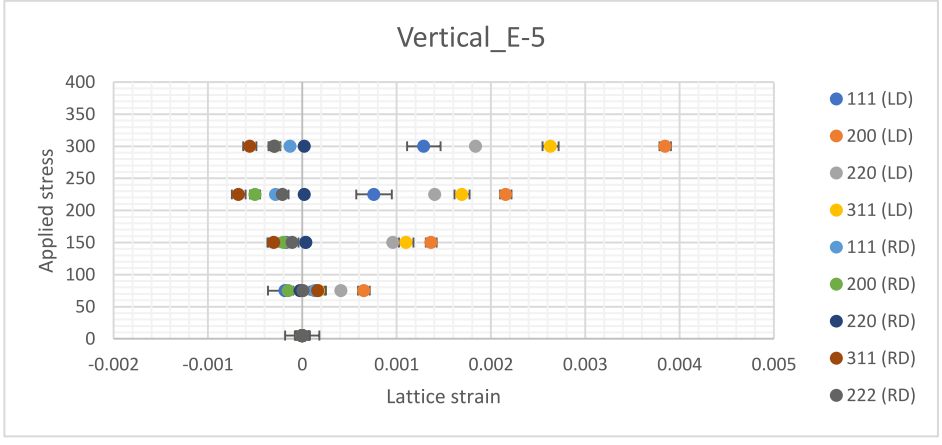

Fig. 5. (a) The true stress – true strain curves of the four different loading conditions during the in-situ neutron measurement. (b)–(e) Lattice strain evolution in both LD and RD at elevated applied stress. Note that the strain uncertainty is determined from the fitting uncertainty in the lattice parameter [50].

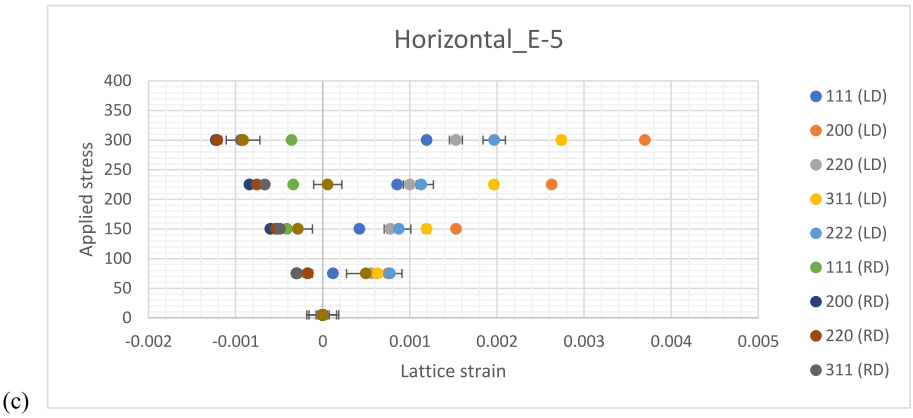

(c)

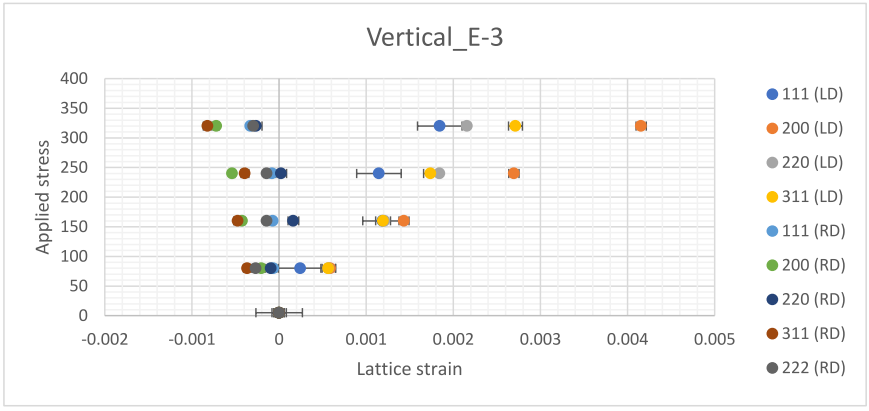

(d)

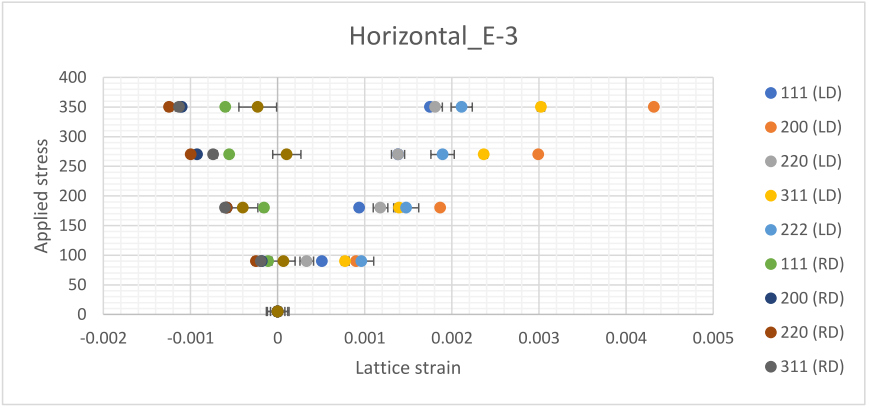

(e)

Fig. 5. (*continued*).

Table 4
The elastic constants of <111>, <200>, <220>, <311> in the loading direction evaluated from Fig. 5b–e. Note that the unit is GPa. Note that E_{200} is fitted within the linear regime as an obvious yielding is observed at the highest applied stress.

	E_{111}	E_{200}	E_{220}	E_{311}
V_E-5	233.3 ± 40.7	102.2 ± 2.1	158.1 ± 3.9	105.6 ± 10.7
H_E-5	230.4 ± 22	84.2 ± 5	204.2 ± 22.7	108.1 ± 3.8
V_E-3	159.4 ± 25.8	85.5 ± 9.5	139.7 ± 8.8	118.2 ± 7.5
H_E-3	198.5 ± 5.5	88.9 ± 2.6	180 ± 19.4	113.5 ± 4

locate at the regime that is either close to the high angle grain boundaries or at the grains that have experienced large texture evolution.

The influence of strain rate on the deformed microstructure in the vertical loading can be compared in Fig. 6c–f. Deformation twins and creep voids are found for both of the strain rates, but the volume fraction is higher in the slow strain rate test. Though V_E-5 shows higher amount of deformation twins (labelled by red lines in Fig. 6d and f), the twin volume fraction is only 1.18%. The deformation twins in V_E-5 are mainly found along the long side of the elongated grains, which are shown in the labelled area in Fig. 6d. For both strain rates, the deformation twins locate at the grains with the crystallographic orientation close to <111>//LD (colour legend of blue). In addition, a texture evolution from <011>//LD to <111>//LD is observed, of which takes place in the grains with texture of <011>//BD in the as-built state. A stronger texture of <111>//LD in the V_E-3, shown in Fig. 6e, implies a higher level of texture evolution, while the V_E-5 fractured before the texture could fully evolve toward <111>//LD.

3. 5Fracture behaviours

The comparison of different fracture behaviours between V_E-5 and H_E-5 is shown in Fig. 7a–d. The vertically loaded sample underwent significant anisotropic contraction, and an oval shape of fracture surface

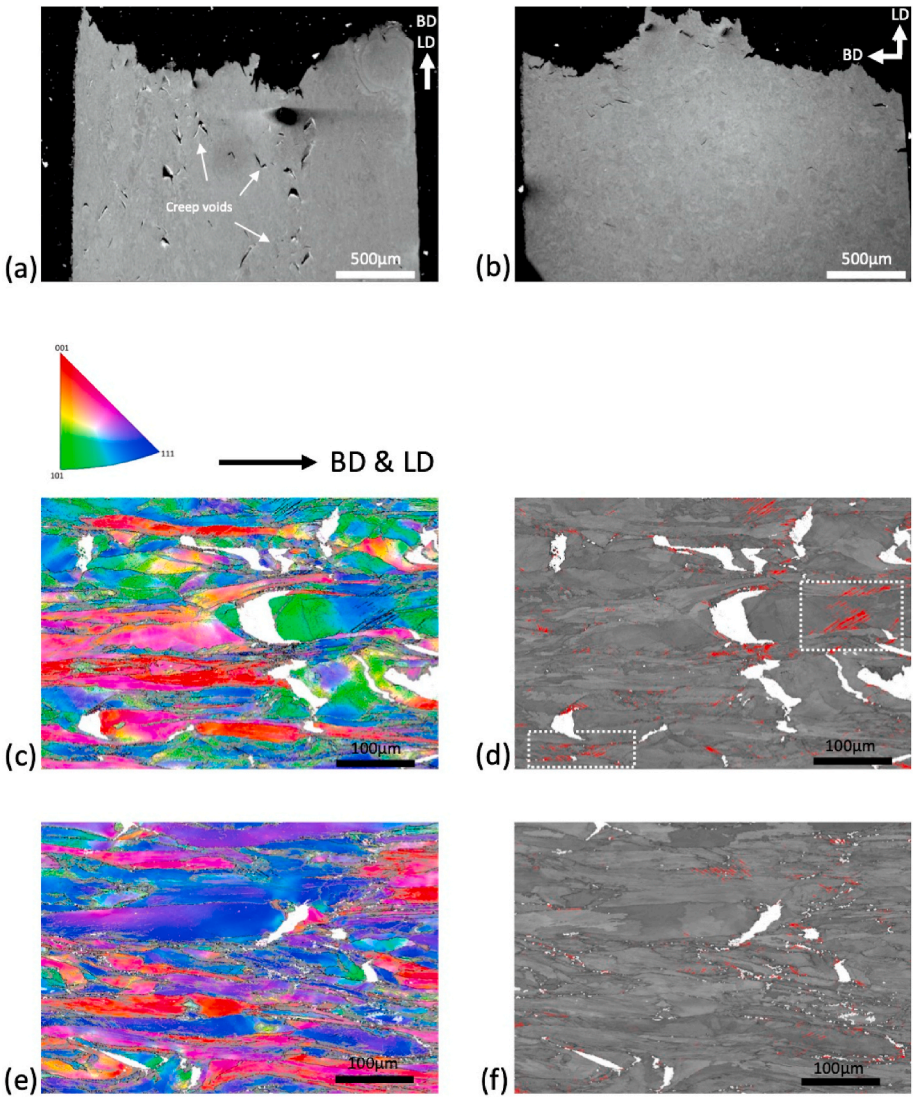

Fig. 6. Microstructures of the specimens deformed at fracture. (a) Deformed microstructure of V_E-5 close to the fracture surface, and the creep voids are indicated. (b) Deformed microstructure of H_E-5 close to the fracture surface. (c)–(d) EBSD grain orientation maps of V_E-5 with different colouring methods. (e)–(f) EBSD grain orientation maps of V_E-3 with different colouring methods. Note that (c)–(f) were taken from the areas that are approximately 1 mm away from the fracture; the BD and LD are along the horizontal direction. The colour legend in (c) and (e) is according to the BD; the scanning step size is 0.5 μm; the black lines refer to >10° grain boundaries, and the grey lines refer to >2° grain boundaries. (d) and (f) are imaged from the band contrast with deformation twins labelled by the red lines. The labelled areas in (d) refer to the long side of the elongated grains with the revealed deformation twins. (For interpretation of the references to colour in this figure legend, the reader is referred to the Web version of this article.)

is found. Intergranular fracture behaviour is observed in both samples, which indicates the creep damages due to the slow strain rate. Multiple directional fractures are shown in Fig. 7c and d, which reveal the directional growth of dendrites that follows the local thermal gradients created during the complex laser movement. The different morphologies of fractures demonstrate the influence of an elongated grain structure. The size of the potholes in the fracture surface of the vertically loaded sample corresponds well with the grain size of the elongated grain structure shown in Fig. 3, and it indicates that the intergranular fracture follows the high angle grain boundaries. The statement is also supported by the observation of creep voids shown in the EBSD mapping from the cross section in Fig. 6. On the other hand, a smoother fracture is observed in the H_E-5 since the loading was applied perpendicular to the long side of the elongated grains. The fracture surfaces of V_E-3 and V_E-5 are shown in Fig. 7e and f. Some of the fracture features in the slow strain rate, such as potholes and directional fracture, can be partially found in the strain rate of 10^{-3}/s. However, higher level of ductile fracture behaviours is observed in the V_E-3 and H_E-3, which are indicated by the dimple fractures.

4. Discussion

4. 1Elastic behaviour

The elastic <hkl>-dependant lattice strain responses upon different loading conditions at 700 °C are shown in Fig. 5. The lattice strain of each grain family with <hkl> aligned in the LD increases with the applied stress, and the slope as a function of the applied stress represents the stiffness of each <hkl> lattice plane, which is summarized in Table 4. For all the different loading conditions, the lattice elastic constant of <111> is found to be the stiffest while <200> is the softest, and the ratio of $E_{<111>}/E_{<200>}$ is about 1.86–2.74. The elastic lattice anisotropy in LPBF HX corresponds well to the theoretical anisotropy [51,52] where the material-dependent ratio of $E_{<111>}/E_{<200>}$ for the pure Ni is 2.36 [53]. The elastic lattice anisotropy agrees well with other in-situ studies of FCC materials, such as Ni-based superalloys [41], austenitic stainless steels [38,54] and high entropy alloys [55]. Moreover, the texture in LPBF HX also leads different degree of lattice anisotropy [56].

In Table 3, the Young's modulus, as average over all (hkl) families with texture taken into account, shows a clear decrease for the slow strain rate, and it indicates an influence of creep deformation also below the yield point [26]. Apparently for the slow strain rate, the micro-plasticity takes place at microstructural defects and grain

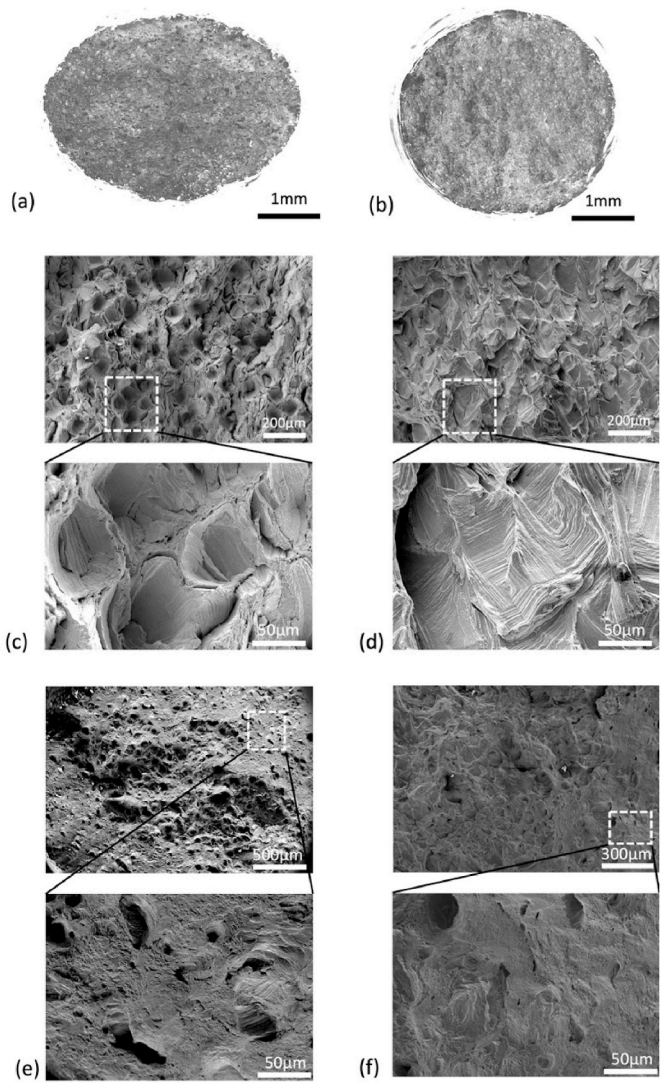

Fig. 7. (a)–(b) Fracture surfaces imaged by using LOM. (a) V_E-5. (b) H_E-5. (c)–(f) Fracture surfaces imaged by using FE-SEM. (c) V_E-5. (d) H_E-5. (e) V_E-3. (f) H_E-3.

boundaries, which is evidenced by the time evolving creep voids at grain boundaries from the deformed microstructure. As a result, the local stress concentration caused by the micro-plasticity can lead to the heterogeneous lattice strain distribution [16,57]. The heterogeneity can be enhanced by the elongated grain structure, the characteristic texture, and the stress-dependent deformation twins around grain boundaries from the deformed microstructure. In Table 4, the variations of the different <hkl> elastic constants are observed between the two strain rates, indicating the strain-rate dependence of the <hkl> elastic constants. The lattice strain obtained by the diffraction pattern only addresses the elastic strain. The strain-rate dependence of the <hkl> elastic constants is assumed to be the result of stress partitioning [31–35], because the micro-plasticity takes place in the macroscopic elastic strain regime and certain crystallographic orientations are prone to yield [31–35]. As the neutron diffraction was averaged over a large volume, the overall variation of elastic constants reveals the strain-rate dependence. Yet, a further study on the microstructural influence on the lattice strain evolution upon creep deformation is required.

The influence of texture on the elastic properties can also be found through texture-based calculations and the difference of Young's modulus between the two loading directions can be confirmed. Fig. 8 presents the estimated Young's modulus surface with the input of as-built bulk texture data obtained from neutron diffractions, a set of single crystal constants and a choice of the model. The Hill's model is applied for the calculation [58]. The input parameters for the calculation were taken from a solid-solution strengthened Ni-based superalloy, Inconel 625. A lattice parameter of 3.6009 Å [59] and the following single crystal constants c_{11} = 205.2 GPa, c_{12} = 149.3 GPa, c_{44} = 99.3 GPa at 700 °C were applied [41]. Due to the existing as-built bulk texture, the Young's modulus shows a certain degree of anisotropy. However, based on the maximum and minimum values, the level of anisotropy is much less than the single crystal. The calculated Young's modulus is 166.6 GPa for the vertical loading, and 125.7 GPa for the horizontal loading. The estimated Young's modulus values corresponds well with the as-built bulk texture shown in Fig. 3c, where the maximum of the Young's modulus can be correlated to the stiffest crystallographic direction <111>. In fact, due to the nature of the as-built texture (single texture component in a Goss orientation), the Young's modulus directional distribution of our textured material is very similar to the single-crystal one (also assuming 45° rotation to the Goss orientation), though of less degree of anisotropy as reported above.

The calculated Young's modulus surface only represents the texture-imposed anisotropy. There are other possible sources of anisotropy such as grain ellipticity. The fact that the Young's modulus for the vertical loading is still found higher than the horizontal loading supports the

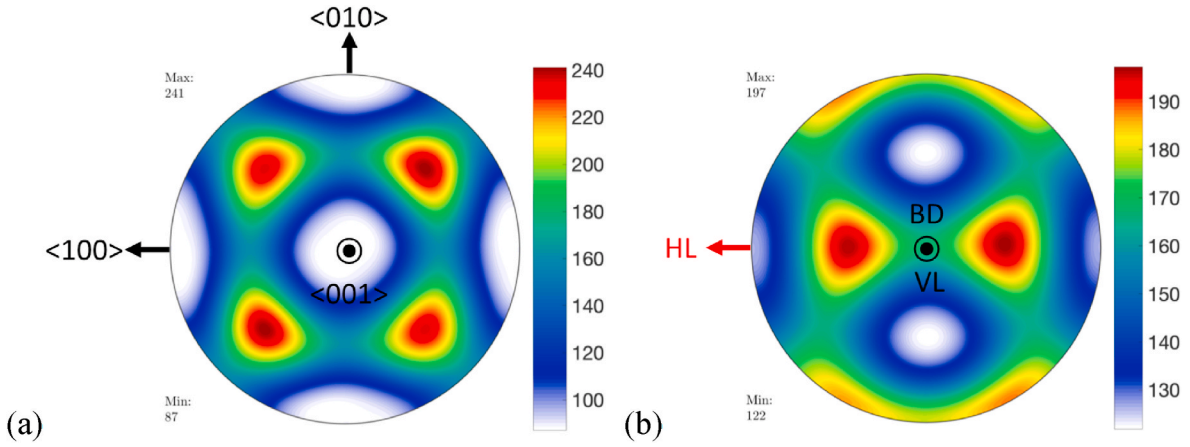

Fig. 8. Estimated Young's modulus surface calculated by using MTEX [60]. The unit is in GPa. (a) Young's modulus surface of a single crystal. (b) Young's modulus surface with the input of as-built LPBF HX texture. The centre of the sphere refers to the vertical loading direction, and the east-west direction refers to the horizontal loading direction.

idea of microstructural influence through crystal texture on the anisotropic Young's modulus.

4.2. Deformation and fracture behaviours

4.2.1. Texture evolution

For the vertical loading, the significantly anisotropic volume contraction shown in Fig. 7a is caused by the large texture evolution and grain rotation. The characteristic contraction direction can be correlated to the as-built texture condition. An EBSD grain orientation map on the cross section of V_E-5 close to the fracture surface is given in Fig. 9. With a simple assumption that it is a constant volume of the gauge section in the tensile specimen,

$$V = A_0 \times L_0 = A_i \times L_i \tag{2}$$

where V is the constant volume of gauge section, A_0 is the original cross-section of the tensile specimen, A_i is the cross section after the deformation, L_0 and L_i are the respective length. The macroscopic strain can be roughly estimated by comparing the original and the deformed cross-section, which is approximately 17%. Roughly equiaxed grain structure is still observed, which is similar to the as-built microstructure shown in Fig. 3. Yet, heterogeneous texture evolution has taken place as less <011>//BD oriented grains are found, leading to reduced preferred orientation. Meanwhile, the radial direction with the largest contraction refers to the X-direction of the pole figures shown in Fig. 9b, where a texture component <001>//X is found at the horizontal poles.

In our previous study, we have observed a large grain rotation and texture evolution in the vertical loading at the strain rate of 10^{-3}/s, which is a merit to the greater vertical ductility compared to the horizontal loading [27]. In this study, the anisotropic ductility is still observed at the strain rate of 10^{-5}/s, and the different behaviour of texture evolution is responsible for the anisotropy as well. The texture evolution estimated from several neutron diffraction peaks upon loading is given in Fig. 10. The first diffraction patterns corresponding to the stress-free state are given in Fig. 10e. The diffraction patterns were measured along the loading direction, where the GOSS texture in the as-built LPBF results in the major peak of (220) in the V_E-5. At the stress-free state in Fig. 10a–d, the pole density (m.r.d, multiples of random distribution) of each <hkl> is determined from the known pole figures of the as-built texture in Fig. 3c, and the texture density evolution is determined as follow,

$$Pole\ density^{*} = Pole\ density^{0} \times \left(\frac{Peak\ intensity^{*}}{Peak\ intensity^{0}}\right) \tag{3}$$

where pole density^0 and pole density* are the density at stress-free state and the corresponding strain; peak intensity*and peak intensity^0 refer to the peak height at the stress-free state and the corresponding strain.

For the vertical loading, a significant decline of (220) after the strain of 0.02 mm/mm is found in both strain rates, which points out the high level of texture evolution. Moreover, the larger drop of (220) in V_E-3 is in line with the higher level of deformation compared to V_E-5 as shown in Fig. 6c and e. On the other hand, a relatively lower intensities variation is found in the horizontal loading, but a clear increase of (111) is revealed in both strain rates. The texture evolution of horizontal loading was found to be close to FCC polycrystalline deformation behaviour [27], where deformed texture components of <001>//LD and <111>//LD are evolved under tension [51]. An increasing tendency of both (200) and (111) in H_E-3 in Fig. 10d corresponds well with the polycrystalline deformation behaviours. However, considering the higher level of increase in (111), a major texture evolution toward <111>//LD is assumed to take place in the horizontal loading.

4.2.2. Creep damage

For the strain rate of 10^{-5}/s, the continuous softening right after the yield point shows clear indication of creep damage. The creep voids at grain boundaries shown in Fig. 6 are evidence of the creep damage. The size of creep voids evolves with time and coalesces with the neighbouring voids, leading to grain boundary decohesion and causing

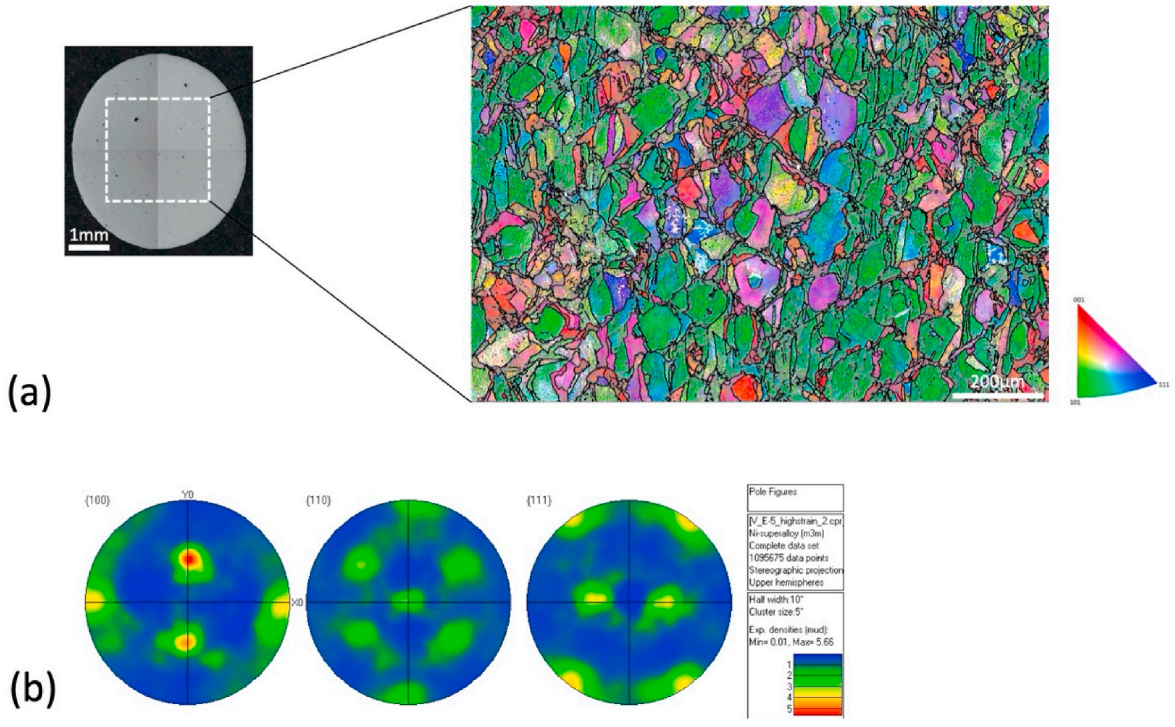

Fig. 9. (a) The cross-section of deformed specimen of V_E-5, and the EBSD grain orientation mapping on the labelled area. Note that the colour legend is according to the BD and the scanning step size is 1 μm. (b) The (100), (110) and (111) pole figures estimated from the EBSD map in (a). (For interpretation of the references to colour in this figure legend, the reader is referred to the Web version of this article.)

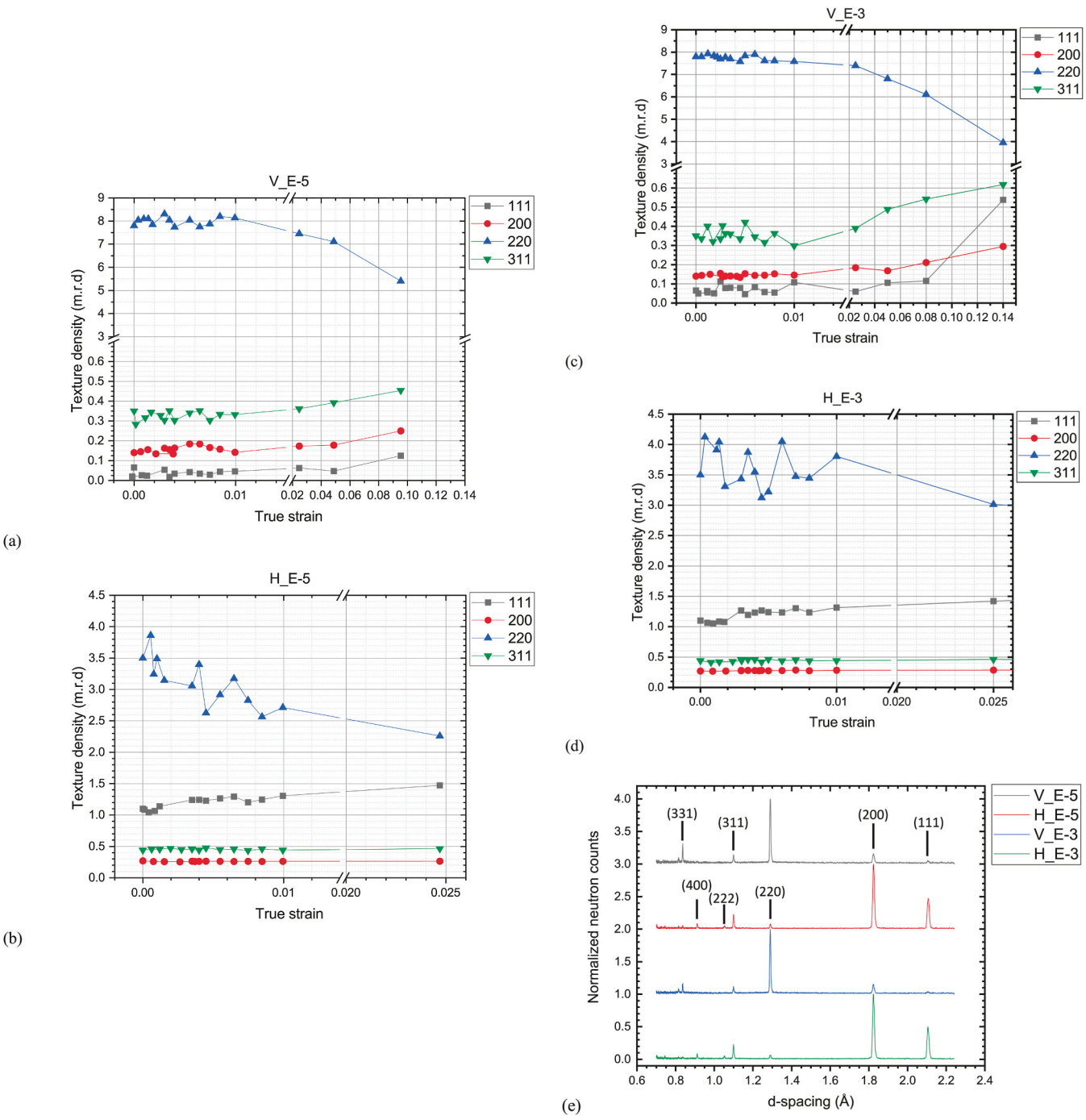

Fig. 10. (a)–(d) give the texture density evolution at elevated strain of V_E-5, H_E-5, V_E-3 and H_E-3, respectively, observed in the in-situ neutron experiment. Note that the texture density evolution is proportional to the peak height evolution of the corresponding peak. (e) The normalized diffraction patterns at the stress-free state before loading.

embrittlement that results in the ductility loss at the slow strain rate. At the testing temperature of 700 °C and for the slow strain rate, the dynamic recovery and localized dynamic recrystallization are also assumed to be responsible for the continuous softening. For the dynamic recovery, the movement of dislocation under plastic deformation releases the stored strain energy and lower the effective work hardening rate [61]. The stress concentration at grain boundaries is expected to induce the localized dynamic recrystallization and further enhances the softening [62]. Judged by the higher level of the softening and the larger amount of the creep voids, the vertical loading is expected to suffer higher level of creep deformation. However, a better vertical ductility is still observed owing to the greater texture evolution and the elongated grain structure. For the horizontal loading, higher amount of grain boundaries is perpendicular to the LD, which is a preferred condition for nucleation and coalescence of creep voids that can accelerate the crack propagation. Therefore, the vertically built specimen is assumed to exhibit better creep resistance, which is also discovered in LPBF stainless steel 316L [63] and Inconel 718 [25,64].

4.2.3. *Creep voids*

The creep void formation is responsible for the inferior ductility at the strain rate of 10^{-5}/s. As the intergranular fracture surfaces are

observed at both the vertical and horizontal loading in Fig. 7, the grain boundaries are clearly embrittled by the creep damage. In addition, the observed secondary cracks along the grain boundaries indicate that the preferred crack formation is along the grain boundaries. Yet, the horizontal ductility is still lower, which is on account of the easier path for crack propagation due to the larger grain boundaries area perpendicular to the LD [65]. The high surface energy on the grain boundaries plays a critical role on the nucleation rate of creep voids [66], and the nucleation rate of creep voids in LPBF materials is expected to be even higher than conventional manufactured materials [25].

Different creep damage behaviours are found between the vertical and the horizontal loading. For the vertical loading, as the LD is applied along the elongated grains, high shear stress is expected in the tangential direction of the long side of grain boundary, which can provide the driving force for grain rotation [67]. At the slow strain rate of 10^{-5}/s, the diffusion-accommodated grain rotation, which includes both lattice diffusion and grain boundaries diffusion, might also need to be considered [68]. However, the vacancy diffusion induced creep void formation is assumed to lessen the tangential shear stress, since the coalescence of creep voids upon loading is speculated to cause grain boundaries sliding and lower the level of grain rotation. Hence, the texture evolution and grain rotation are lower at the slow strain rate, as indicated in Fig. 6c and e. On the other hand, at the short side of the elongated grains, a higher level of grain boundary detachment is expected due to the higher normal stress on the grain boundaries, and the sharper curvature on the short side that is possible to trigger more vacancy diffusion. The evidence can be found in Fig. 6a and c, where roughly a "V" shape distribution of creep voids is revealed, and they locate at the grains that have been through large texture evolution and are with high misorientation to the neighbouring grains. The "V" shape of creep voids correlates well with the "pothole" on the fracture surface of V_E-5 shown in Fig. 7c. Higher amount of creep voids can be found from the cross-section in the vertical loading compared to the horizontal loading in Fig. 6a and b. It is assumed that the grain boundaries in the vertical loading cannot accommodate such high level of grain rotation, therefore, large creep voids are created. By contrast, the creep damage is mainly developed along the major fracture in the horizontal loading, which results in the lower amount of creep voids in the cross-section.

4.2.4. Deformation twinning

Deformation twinning is a stress-dependent deformation mechanism that can be dominant at low temperature or at high strain rate [69]. The critical stress for twinning is determined by the crystallographic orientation, where the relation of critical stress, $\sigma_{<011>} < \sigma_{<111>} < \sigma_{<001>}$ can be found [30,70,71]. Yet, the deformation twins are found at the grains with the crystallographic orientation close to <111>//LD instead of <011>//LD in Fig. 6. It is speculated that the twinning process still takes place at the grains with <011>//LD texture, which is the orientation requiring the least stress for twinning, but the twinned grains undergo grain rotation and become <111>//LD at the fully deformed microstructure. Another speculation is that the deformation twins are triggered by the stress triaxiality [72], where a high level of stress triaxiality is expected in the plastic deformation as an evident necking was observed.

On the effect of elevated temperature, cross slips and multiple slip systems are expected to be activated that can become an easier deformation path than twinning. Therefore, although deformation twinning in LPBF HX has been reported at room temperature [29,30] a low twin volume fraction is revealed in this study. On the effect of slow strain rate, the formation of creep voids combined with the tangential shear stress at the long sides of elongated grains is presumed to induce stress concentration at grain boundaries, which can trigger deformation twinning [73]. The formation of deformation twins provides an alternative deformation path for dislocation movement, which can be beneficial to the ductility. However, considering the low twin volume fraction, it is assumed that the texture evolution plays a more critical role in the anisotropic ductility.

4.3. The role of texture in ductility

The anisotropic texture evolution greatly influences the ductility under different loading conditions, and the initial texture of the as-built specimen actually plays a big role for the vertical ductility. In our previous work [27,28], we have studied the plate-like specimens of LPBF HX with the similar manufacturing process. Compared to the present work, we observe a ductility difference between the plate-like and rod-like tensile specimens due to the different level of initial texture and grain size, see Fig. 11. The plate-like specimen texture distribution type is rather close to <011>//BD fibre texture, while for the bulk sample the main feature that <011>//BD is pertained in a different orientation, not through fibre component, but through Goss texture component. The sharpness of texture is much weaker in the plate-like sample than the bulk, rod-like specimen. In addition, a smaller grain size and aspect ratio is found in the plate-like specimen from the cross section that is normal to the LD.

GOSS texture with elongated grain structure and high dislocation density in LPBF HX show similarity with rolled materials [74–76]. The high dislocation density in rolled materials promotes dynamic recrystallization when heat treatment is applied, and the dynamic recrystallization further leads to texture evolution, specifically forming Goss component. The cyclic heat exposure in LPBF process induces dynamic recovery, dynamic recrystallization and possible grain growth at different thermal cycles [77], which is assumed to cause the different textures observed in the bulk rod-like and plate-like specimen. With the similar LPBF process, the geometry and size of specimen are expected to be responsible for the texture difference. The plate-like specimen has smaller cross-section for the hatching, and a faster heat dissipation toward the powder bed is presumed. Meanwhile, a larger grain size of the bulk rod-like specimen indicates the higher degree of grain growth, since the high temperature in the hatching cross-section can be retained longer. For the bulk rod-like specimen, one might also question the asymmetric texture component of GOSS texture in the in-plane direction normal to the BD, because a symmetric in-plane thermal gradient is expected as 67° scan rotation has been applied. The dynamic recrystallization during the cyclic heat exposure is suspected to lead to the GOSS texture in LPBF HX, which resembles the texture evolution under heat treatment in some rolled materials. The higher level of grain growth in the rod-like specimen further strengthens the GOSS texture.

A strong crystallographic-dependent tensile behaviour has been reported in LPBF face-centred cubic (FCC) materials [30,78], where the <011> orientation shows better ductility compared to <001> and <111> orientations. From the creep study on single crystal Ni-based superalloys at elevated temperatures, a better ductility can also be found in the <011> orientation [79,80], which is due to large lattice rotation via the easily activated <011>{111} slip system. Back to our observation, it is assumed that the <011>//BD fibre texture with lower texture level in the plate-like specimen is beneficial for activating the <011>{111} slip system, because multiple slips can be activated with less confinement compared to the strong GOSS texture. Furthermore, the smaller grain size with the lower aspect ratio of the plate-like specimen is also expected to be advantageous to the better ductility since the grain rotation is easier to be accommodated without leading to fracture during the grain-to-grain interaction. In summary, the GOSS texture with higher intensity and the larger grain size of the rod-like specimen are responsible for the lower ductility.

5. Conclusions

This work is an in-depth study on the anisotropic tensile deformation mechanisms of LPBF HX at elevated temperature. It is an investigation on the LPBF HX produced with the standard process parameters using EOS M290 equipment, which is a commonly used process in LPBF. It is

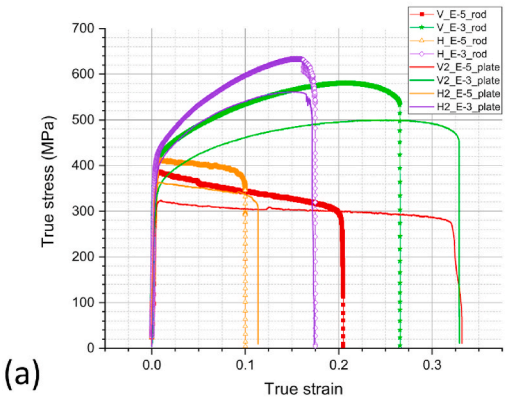

(a)

Sample	Ductility
V_E-5_rod	23%
V_E-3_rod	30%
H_E-5_rod	11%
H_E-3_rod	19%
V_E-5_plate	39%
V_E-3_plate	39%
H_E-5_plate	12%
H_E-3_plate	19%

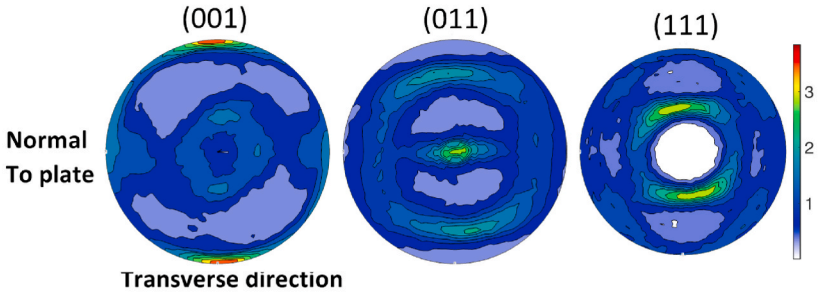

(b)

(c)

	Grain size (μm)	Aspect ratio
Rod	24.6	2.8
Plate	16.8	2.5

Fig. 11. Ductility comparison to the plate-like tensile specimens from the previous study [27,28]. (a) The stress-strain curves of the rod-like specimens in this study and the plate-like specimens in the previous study. The table summarizes the ductility, which refers to the strain at the fracture. (b) The pole figures (100), (110) and (111) of the plate-like specimen. (c) The grain size and aspect ratio determined from the cross section that is normal to the LD, which is the cross section revealing the roughly equiaxed grain structure of the elongated grains, and the grain size lower than 5 μm has been filtered out from the determination.

aimed to study the influence of the characteristic microstructures occurring in LPBF on the anisotropic mechanical behaviours. A 2x2 matrix of tensile loading conditions were examined: the vertical loading and the horizontal loading at two different strain rates, 10^{-5}/s and 10^{-3}/s. The slower strain rate was applied for the purpose of probing the short-term creep behaviours. In-situ time-of-flight neutron diffraction upon loading was performed to track the lattice strain and texture evolution. The investigation is combined with post microstructure analysis on the specimens that were deformed to failure. The following conclusions are drawn from this work:

- The microstructure of HX as produced in the standard production route by LPBF is anisotropic in terms of the grain shape and orientation. The grain preferred orientation is <011>//BD, while the texture is characterized by the strong Goss texture component with certain ellipticity of its distribution. The direct consequence of the preferred orientation is the anisotropy of the elastic properties, i.e. Young's modulus, that was experimentally determined and estimated through ODF-based calculations.
- Anisotropic tensile properties are present for both strain rates at 700 °C, where a weaker strength but better ductility is observed in the vertical loading due to the strong GOSS texture. At the slow strain rate of 10^{-5}/s, a continuous softening right after the yielding is shown in both loading types, which is due to the creep damage. The grain boundary embrittlement caused by creep void formation is observed in both loading types, but the anisotropic fracture mechanism is shown. The vertical loading is assumed to perform better creep resistance.
- Lattice strain evolutions for the <111>, <200>, <220> and <311> crystal directions were traced in both loading directions. For the slow strain rate of 10^{-5}/s, the bulk Young's modulus is lower while the lattice elastic constants of <111> and <220> increase significantly for both sample directions. For the lattice elastic constant of <200>, it only increases in the vertical loading direction at the slow strain rate. The micro-plasticity at the slow strain rate causes the heterogeneity of lattice strain distribution, which leads to the strain-rate dependence of the <hkl> elastic constants.
- High degree of texture evolution and grain rotation is observed in the vertical loading direction, which results in the better vertical ductility for both strain rates. In addition, deformation twins are also only observed in the vertical loading, which can provide an alternative deformation path and contribute to the better ductility. The twinning deformation mechanism is more pronounced in slow strain rates since a higher twin volume fraction is observed for the slow strain rate. However, considering the low twin fraction of 1.18%, it is assumed that the texture evolution and grain rotation play a more critical role in the anisotropic ductility. For the horizontal loading, a relative lower level of texture evolution is exhibited, and a texture evolution toward <111>//LD is traced.
- From a comparison to the previous study of plate-like LPBF HX specimens, the rod-like specimen in this study shows stronger GOSS texture and larger grain size. The dynamic recrystallization during cyclic heat exposure in LPBF is assumed to lead to the GOSS texture, and the higher level of grain growth in the rod-like specimen leads to the larger grain size and strengthens the GOSS texture. The

difference in microstructure and texture leads to the lower ductility of the rod-like LPBF HX samples for both strain rates.

CRediT authorship contribution statement

Cheng-Han Yu: Conceptualization, Methodology, Validation, Investigation, Data curation, Writing – original draft, Writing – review & editing, Visualization, Project administration. **Ru Lin Peng:** Conceptualization, Writing – review & editing. **Tung Lik Lee:** Methodology, Validation, Investigation, Data curation, Writing – review & editing. **Vladimir Luzin:** Methodology, Validation, Investigation, Writing – review & editing. **Jan-Erik Lundgren:** Writing – review & editing. **Johan Moverare:** Conceptualization, Supervision, Funding acquisition, Methodology, Writing – review & editing.

Declaration of competing interest

The authors declare that they have no known competing financial interests or personal relationships that could have appeared to influence the work reported in this paper.

Acknowledgement

This study was supported by the Swedish Governmental Agency for Innovation Systems (Vinnova grant 2016-05175) and the Centre for Additive Manufacturing-metal (CAM^2). Support from AFM at Linköping University and the faculty grant SFO-MATLiU#2009-00971 is also acknowledged. Experiments at the ISIS Neutron and Muon Source were supported by a beamtime allocation RB2010043 from the Science and Technology Facilities Council [44].

All the data in this study are available from the corresponding author on reasonable request.

References

[1] R.C. Reed, The Superalloys. Fundamentals and Applications, Cambridge University Press, 2006.
[2] C.Y. Yap, et al., Review of selective laser melting: materials and applications, Appl. Phys. Rev. 2 (4) (2015), https://doi.org/10.1063/1.4935926.
[3] T. DebRoy, et al., Additive manufacturing of metallic components – process, structure and properties, Prog. Mater. Sci. 92 (2018) 112–224, https://doi.org/10.1016/j.pmatsci.2017.10.001.
[4] D. Herzog, V. Seyda, E. Wycisk, C. Emmelmann, Additive manufacturing of metals, Acta Mater. 117 (2016) 371–392, https://doi.org/10.1016/j.actamat.2016.07.019.
[5] O. Andersson, A. Graichen, H. Brodin, V. Navrotsky, Developing additive manufacturing technology for burner repair, J. Eng. Gas Turbines Power 139 (3) (2016), 031506, https://doi.org/10.1115/1.4034235.
[6] J. Zhao, M. Larsen, V. Ravikumar, Phase precipitation and time – temperature-transformation diagram of Hastelloy X, Mater. Sci. Eng., A 293 (2000) 112–119.
[7] A.K. Bhattacharya, et al., High-temperature tensile-hold crack-growth behavior of HASTELLOY® X alloy compared to HAYNES® 188 and HAYNES® 230® alloys, Mech. Time-Dependent Mater. 12 (1) (2008) 31–44, https://doi.org/10.1007/s11043-008-9049-6.
[8] A. Shaji Karapuzha, et al., Microstructure, mechanical behaviour and strengthening mechanisms in Hastelloy X manufactured by electron beam and laser beam powder bed fusion, J. Alloys Compd. 862 (2021), 158034, https://doi.org/10.1016/j.jallcom.2020.158034.
[9] O. Gokcekaya, T. Ishimoto, S. Hibino, J. Yasutomi, T. Narushima, T. Nakano, Unique crystallographic texture formation in Inconel 718 by laser powder bed fusion and its effect on mechanical anisotropy, Acta Mater. 212 (2021), 116876, https://doi.org/10.1016/j.actamat.2021.116876.
[10] P. Karimi, et al., Columnar-to-equiaxed grain transition in powder bed fusion via mimicking casting solidification and promoting in situ recrystallization, Addit. Manuf. 46 (2021), 102086, https://doi.org/10.1016/j.addma.2021.102086.
[11] A. Leicht, C.H. Yu, V. Luzin, U. Klement, E. Hryha, Effect of scan rotation on the microstructure development and mechanical properties of 316L parts produced by laser powder bed fusion, Mater. Char. 163 (2020), 110309, https://doi.org/10.1016/j.matchar.2020.110309.
[12] A. Keshavarzkermani, et al., Controlling mechanical properties of additively manufactured hastelloy X by altering solidification pattern during laser powder-bed fusion, Mater. Sci. Eng., A 762 (2019), 138081, https://doi.org/10.1016/j.msea.2019.138081.
[13] W.G. Kim, S.N. Yin, Y.W. Kim, J.H. Chang, Creep characterization of a Ni-based Hastelloy-X alloy by using theta projection method, Eng. Fract. Mech. 15 (17) (2008) 4985–4995, https://doi.org/10.1016/j.engfracmech.2008.06.017.
[14] W.G. Kim, S.N. Yin, W.S. Ryu, J.H. Chang, S.J. Kim, Tension and creep design stresses of the 'Hastelloy-X' alloy for high-temperature gas cooled reactors, Mater. Sci. Eng., A 483–484 (2008) 495–497, https://doi.org/10.1016/j.msea.2006.12.184.
[15] S. Hayashi, M. Sakata, S. Ukai, T. Narita, Creep deformation/oxidation behavior of Re-Cr-Ni diffusion barrier coated hastelloy-X at 970°C in air, Mater. Sci. Forum 59 (6) (2008) 471–475. https://doi.org/10.4028/www.scientific.net/msf.595-598.107.
[16] W.Z. Abuzaid, H. Sehitoglu, J. Lambros, W.Z. Abuzaid, H. Sehitoglu, J. Lambros, Localisation of plastic strain at the microstructural level in Hastelloy X subjected to monotonic , fatigue , and creep loading : the role of grain boundaries and slip transmission, Mater. A. T. High. Temp. 3409 (2016) 1–17, https://doi.org/10.1080/09603409.2016.1152421.
[17] S. Banoth, T.N. Palleda, S. Shimazu, K. Kakehi, Yttrium's effect on the hot cracking and creep properties of a ni-based superalloy built up by additive manufacturing, Materials 14 (5) (2021) 1143, https://doi.org/10.3390/ma14051143.
[18] N.J. Harrison, I. Todd, K. Mumtaz, Reduction of micro-cracking in nickel superalloys processed by Selective Laser Melting: a fundamental alloy design approach, Acta Mater. 94 (2015) 59–68, https://doi.org/10.1016/j.actamat.2015.04.035.
[19] F. Wang, Mechanical property study on rapid additive layer manufacture Hastelloy® X alloy by selective laser melting technology, Int. J. Adv. Manuf. Technol. 58 (2012) 545–551, https://doi.org/10.1007/s00170-011-3423-2.
[20] O. Sanchez-Mata, J.A. Muñiz-Lerma, X. Wang, S.E. Atabay, M. Attarian Shandiz, M. Brochu, Microstructure and mechanical properties at room and elevated temperature of crack-free Hastelloy X fabricated by laser powder bed fusion, Mater. Sci. Eng., A 780 (2020), 139117, https://doi.org/10.1016/j.msea.2020.139177.
[21] D. Tomus, P.A. Rometsch, M. Heilmaier, X. Wu, Effect of minor alloying elements on crack-formation characteristics of Hastelloy-X manufactured by selective laser melting, Addit. Manuf. 16 (2017) 65–72, https://doi.org/10.1016/j.addma.2017.05.006.
[22] M.L. Montero-Sistiaga, et al., Effect of temperature on the microstructure and tensile properties of micro-crack free hastelloy X produced by selective laser melting, Addit. Manuf. 31 (2020), 100995, https://doi.org/10.1016/j.addma.2019.100995. December 2019.
[23] C.H. Yu, R. Peng, J.E. Lundgren, J. Moverare, Anisotropic Mechanical Properties of Thin-Walled Hastelloy X Manufactured by Laser Powder Bed Fusion, 2019.
[24] J. Xu, H. Gruber, D. Deng, R.L. Peng, J.J. Moverare, Short-term creep behavior of an additive manufactured non-weldable Nickel-base superalloy evaluated by slow strain rate testing, Acta Mater. 179 (2019) 142–157, https://doi.org/10.1016/j.actamat.2019.08.034. August.
[25] D. Deng, R.L. Peng, J. Moverare, High temperature mechanical integrity of selective laser melted alloy 718 evaluated by slow strain rate tests, Int. J. Plast. 140 (2021), 102974, https://doi.org/10.1016/j.ijplas.2021.102974.
[26] V. Norman, M. Calmunger, An accelerated creep assessment method based on inelastic strain partitioning and slow strain rate testing, Mater. Des. 205 (2021), 109697, https://doi.org/10.1016/j.matdes.2021.109697.
[27] C.H. Yu, et al., Thin-wall effects and anisotropic deformation mechanisms of an additively manufactured Ni-based superalloy, Addit. Manuf. 36 (2020), 101672, https://doi.org/10.1016/j.addma.2020.101672.
[28] C.-H. Yu, R.L. Peng, M. Calmunger, V. Luzin, H. Brodin, J. Moverare, Anisotropic deformation and fracture mechanisms of an additively manufactured Ni-based superalloy, in: TMS Superalloys vol. 2020, 2020, pp. 1003–1013, https://doi.org/10.1007/978-3-030-51834-9_98.
[29] R. Ghiaasiaan, M. Muhammad, P.R. Gradl, S. Shao, N. Shamsaei, Superior tensile properties of Hastelloy X enabled by additive manufacturing, Mater. Res. Lett. 9 (7) (2021) 308–314, https://doi.org/10.1080/21663831.2021.1911870.
[30] O. Sanchez-Mata, X. Wang, J.A. Muñiz-Lerma, S.E. Atabay, M. Attarian Shandiz, M. Brochu, Dependence of mechanical properties on crystallographic orientation in nickel-based superalloy Hastelloy X fabricated by laser powder bed fusion, J. Alloys Compd. 865 (2021), 158868, https://doi.org/10.1016/j.jallcom.2021.158868.
[31] M. Ojima, et al., Stress partitioning behavior of multilayered steels during tensile deformation measured by in situ neutron diffraction, Scripta Mater. 66 (3–4) (2012) 139–142, https://doi.org/10.1016/j.scriptamat.2011.10.018.
[32] W. Woo, V.T. Em, E.Y. Kim, S.H. Han, Y.S. Han, S.H. Choi, Stress-strain relationship between ferrite and martensite in a dual-phase steel studied by in situ neutron diffraction and crystal plasticity theories, Acta Mater. 60 (20) (2012) 6972–6981, https://doi.org/10.1016/j.actamat.2012.08.054.
[33] D.K. Kim, W. Woo, J.H. Hwang, K. An, S.H. Choi, Stress partitioning behavior of an AlSi10Mg alloy produced by selective laser melting during tensile deformation using in situ neutron diffraction, J. Alloys Compd. 686 (2016) 281–286, https://doi.org/10.1016/j.jallcom.2016.06.011.
[34] J. Coakley, R.C. Reed, J.L.W. Warwick, K.M. Rahman, D. Dye, Lattice strain evolution during creep in single-crystal superalloys, Acta Mater. 60 (6–7) (2012) 2729–2738, https://doi.org/10.1016/j.actamat.2012.01.039.
[35] S. Huang, et al., Deformation mechanisms in a precipitation-strengthened ferritic superalloy revealed by in situ neutron diffraction studies at elevated temperatures, Acta Mater. 83 (2015) 137–148, https://doi.org/10.1016/j.actamat.2014.09.053.
[36] B. Cai, et al., Deformation mechanisms of Mo alloyed FeCoCrNi high entropy alloy: in situ neutron diffraction, Acta Mater. 127 (2017) 471–480, https://doi.org/10.1016/j.actamat.2017.01.034.
[37] O. Muránsky, C.J. Hamelin, V.I. Patel, V. Luzin, C. Braham, The influence of constitutive material models on accumulated plastic strain in finite element weld analyses, Int. J. Solid Struct. 69 (70) (2015) 518–530, https://doi.org/10.1016/j.ijsolstr.2015.04.032.

[38] J.S. Jeong, W. Woo, K.H. Oh, S.K. Kwon, Y.M. Koo, In situ neutron diffraction study of the microstructure and tensile deformation behavior in Al-added high manganese austenitic steels, Acta Mater. 60 (5) (2012) 2290–2299, https://doi.org/10.1016/j.actamat.2011.12.043.
[39] R.B. Von Dreele, J.D. Jorgensen, C.G. Windsor, Rietveld refinement with spallation neutron powder diffraction data, J. Appl. Crystallogr. 15 (1982) 581–589, https://doi.org/10.1107/s0021889882012722.
[40] M.R. Daymond, N.W. Bonner, Lattice strain evolution in IMI 834 under applied stress, Mater. Sci. Eng., A 340 (1–2) (2003) 272–280, https://doi.org/10.1016/S0921-5093(02)00183-1.
[41] Z. Wang, A.D. Stoica, D. Ma, A.M. Beese, Diffraction and single-crystal elastic constants of Inconel 625 at room and elevated temperatures determined by neutron diffraction, Mater. Sci. Eng., A 674 (2016) 406–412, https://doi.org/10.1016/j.msea.2016.08.010.
[42] C.-H. Yu, Anisotropic Mechanical Behaviors and Microstructural Evolution of Thin-Walled Additively Manufactured Metals, Linköping University Electronic Press, 2020.
[43] J.R. Santisteban, M.R. Daymond, J.A. James, L. Edwards, ENGIN-X: a third-generation neutron strain scanner, J. Appl. Crystallogr. 39 (2006) 821–825, https://doi.org/10.1107/S0021889806042245.
[44] J. Moverare, R.L. Peng, C.-H. Yu, T.L. Lee, In-situ Neutron Diffraction Study: High Temperature Anisotropic Deformation Mechanism of Ni-Based Superalloy Built by Additive Manufacturing, STFC ISIS Neutron and Muon Source, 2020, https://doi.org/10.5286/ISIS.E.RB2010043.
[45] C.M. Moreton-Smith, S.D. Johnston, F.A. Akeroyd, Open GENIE-a generic multi-platform program for the analysis of neutron scattering data, J. Neutron Res. 4 (1996) 41–47, https://doi.org/10.1080/10238169608200066.
[46] Sample geometry in ENGIN-X stress rig. https://www.isis.stfc.ac.uk/Pages/ENGINX-Stress-rig.aspx.
[47] A. Brule, O. Kirstein, Residual stress diffractometer KOWARI at the Australian research reactor OPAL: status of the project, Phys. B Condens. Matter 385–386 (2006) 1040–1042, https://doi.org/10.1016/j.physb.2006.05.333.
[48] R. Hielscher, H. Schaeben, A novel pole figure inversion method: specification of the MTEX algorithm, J. Appl. Crystallogr. 41 (6) (2008) 1024–1037, https://doi.org/10.1107/S0021889808030112.
[49] M. Bahshwan, C.W. Myant, T. Reddyhoff, M.S. Pham, The role of microstructure on wear mechanisms and anisotropy of additively manufactured 316L stainless steel in dry sliding, Mater. Des. 196 (2020), 109076, https://doi.org/10.1016/j.matdes.2020.109076.
[50] R.C. Wimpory, C. Ohms, M. Hofmann, R. Schneider, A.G. Youtsos, Statistical analysis of residual stress determinations using neutron diffraction, Int. J. Pres. Ves. Pip. 86 (1) (2009) 48–62, https://doi.org/10.1016/j.ijpvp.2008.11.003.
[51] W.F. Hosford, Mechanical Behavior of Materials, Cambridge University Press, 2005.
[52] R.W. Hertzberg, Deformation and Fracture Mechanics of Engineering, John Wiley & Sons, INC., 1996.
[53] W.F. Hosford, The Mechanics of Crystals and Textured Polycrystals, Oxford University Press, USA, 1993.
[54] K. An, H.D. Skorpenske, A.D. Stoica, D. Ma, X.L. Wang, E. Cakmak, First in situ lattice strains measurements under load at VULCAN, Metall. Mater. Trans. 42 (2011) 95–99, https://doi.org/10.1007/s11661-010-0495-9.
[55] B. Cai, et al., Deformation mechanisms of Mo alloyed FeCoCrNi high entropy alloy: in situ neutron diffraction, Acta Mater. 127 (2017) 471–480, https://doi.org/10.1016/j.actamat.2017.01.034.
[56] U.F. Kocks, C.N. Tomé, H.R. Wenk, Texture and Anisotropy: Preferred Orientations in Polycrystals and Their Effect on Materials Properties, Cambridge university press, 2000.
[57] G.J. Pataky, H. Sehitoglu, Experimental methodology for studying strain heterogeneity with microstructural data from high temperature deformation, Exp. Mech. 55 (2015) 53–63, https://doi.org/10.1007/s11340-014-9926-7.
[58] R. Hill, The elastic behaviour of a crystalline aggregate, Proc. Phys. Soc. 65 (1952) 349, https://doi.org/10.1088/0370-1298/65/5/307.
[59] F. Zhang, et al., Effect of heat treatment on the microstructural evolution of a nickel-based superalloy additive-manufactured by laser powder bed fusion, Acta Mater. 152 (2018) 200–214, https://doi.org/10.1016/j.actamat.2018.03.017.
[60] D. Mainprice, R. Hielscher, H. Schaeben, Calculating anisotropic physical properties from texture data using the MTEX open-source package, Geol. Soc. Spec. Publ. 360 (2011) 175–192, https://doi.org/10.1144/SP360.10.
[61] R. Abbaschian, L. Abbaschian, R.E. Reed-Hill, Physical Metallurgy Principles, fourth ed., Cengage Learning, 2009.
[62] L.H. Rettberg, T.M. Pollock, Localized recrystallization during creep in nickel-based superalloys GTD444 and René N5, Acta Mater. 73 (2014) 287–297, https://doi.org/10.1016/j.actamat.2014.03.052.
[63] R.J. Williams, J. Al-Lami, P.A. Hooper, M.S. Pham, C.M. Davies, Creep deformation and failure properties of 316 L stainless steel manufactured by laser powder bed fusion under multiaxial loading conditions, Addit. Manuf. 37 (2021), 101706, https://doi.org/10.1016/j.addma.2020.101706. July 2020.
[64] S. Sanchez, G. Gaspard, C.J. Hyde, I.A. Ashcroft, G.A. Ravi, A.T. Clare, The creep behaviour of nickel alloy 718 manufactured by laser powder bed fusion, Mater. Des. 204 (2021), 109647, https://doi.org/10.1016/j.matdes.2021.109647.
[65] D. Deng, R.L. Peng, J. Moverare, On the dwell-fatigue crack propagation behavior of a high strength superalloy manufactured by electron beam melting, Mater. Sci. Eng., A 760 (2019) 448–457, https://doi.org/10.1016/j.msea.2019.06.013.
[66] R. Raj, M.F. Ashby, Intergranular fracture at elevated temperature, Acta Metall. 23 (6) (1975) 653–666, https://doi.org/10.1016/0001-6160(75)90047-4.
[67] J.W. Cahn, J.E. Taylor, A unified approach to motion of grain boundaries, relative tangential translation along grain boundaries, and grain rotation, Acta Mater. 52 (16) (2004) 4887–4898, https://doi.org/10.1016/j.actamat.2004.02.048.
[68] D. Moldovan, D. Wolf, S.R. Phillpot, Theory of diffusion-accommodated grain rotation in columnar polycrystalline microstructures, Acta Mater. 49 (17) (2001) 3521–3532, https://doi.org/10.1016/S1359-6454(01)00240-3.
[69] G.E. Dieter, D.J. Bacon, Mechanical Metallurgy, McGraw-hill, New York, 1986.
[70] T.S. Byun, On the stress dependence of partial dislocation separation and deformation microstructure in austenitic stainless steels, Acta Mater. 51 (11) (2003) 3063–3071, https://doi.org/10.1016/S1359-6454(03)00117-4.
[71] C.-H. Yu, R.L. Peng, H. Brodin, J. Moverare, Anisotropic deformation and fracture mechanisms of an additively manufactured Ni-based superalloy, in: TMS Superalloys vol. 2020, 2020, pp. 1003–1013.
[72] J.B. le Graverend, F. Pettinari-Sturmel, J. Cormier, M. Hantcherli, P. Villechaise, J. Douin, Mechanical twinning in Ni-based single crystal superalloys during multiaxial creep at 1050 °C, Mater. Sci. Eng., A 722 (2018) 76–87, https://doi.org/10.1016/j.msea.2018.02.086.
[73] I. Gutierrez-Urrutia, D. Raabe, Grain size effect on strain hardening in twinning-induced plasticity steels, Scripta Mater. 66 (12) (2012) 992–996, https://doi.org/10.1016/j.scriptamat.2012.01.037.
[74] Z. Gao, Z. Jia, J. Ji, D. Liu, T. Guo, Y. Ding, Texture evolution and dislocation behavior in a nickel-based superalloy during hot compression, Adv. Eng. Mater. 22 (3) (2020) 1–9, https://doi.org/10.1002/adem.201900892.
[75] M. Demura, Y. Xu, T. Hirano, Texture memory effect in heavily cold-rolled Ni_3Al single crystals, Mater. Sci. Forum 539 (543) (2007) 1513–1518. https://doi.org/10.4028/www.scientific.net/msf.539-543.1513.
[76] Y. Cao, X. Shen, H. Di, G. Huang, Texture and microstructure evolution of Incoloy 800H superalloy during hot rolling and solution treatment, J. Alloys Compd. 698 (2017) 304–316, https://doi.org/10.1016/j.jallcom.2016.12.174.
[77] H.E. Sabzi, et al., Grain refinement in laser powder bed fusion: the influence of dynamic recrystallization and recovery, Mater. Des. 196 (2020), 109181, https://doi.org/10.1016/j.matdes.2020.109181.
[78] X. Wang, J.A. Muñiz-Lerma, M. Attarian Shandiz, O. Sanchez-Mata, M. Brochu, Crystallographic-orientation-dependent tensile behaviours of stainless steel 316L fabricated by laser powder bed fusion, Mater. Sci. Eng., A 766 (2019), 138395, https://doi.org/10.1016/j.msea.2019.138395.
[79] L. Cao, P. Thome, L. Agudo Jácome, C. Somsen, G. Cailletaud, G. Eggeler, On the influence of crystallography on creep of circular notched single crystal superalloy specimens, Mater. Sci. Eng., A 782 (2020), 139255, https://doi.org/10.1016/j.msea.2020.139255.
[80] M.G. Ardakani, M. McLean, B.A. Shollock, Twin formation during creep in single crystals of nickel-based superalloys, Acta Mater. 47 (9) (1999) 2593–2602, https://doi.org/10.1016/S1359-6454(99)00145-7.